Lab on a Chip

PAPER

View Article Online
View Journal | View Issue

Cite this: *Lab Chip*, 2021, **21**, 4779

A method of sequential liquid dispensing for the multiplexed genetic diagnosis of viral infections in a microfluidic device†

Daigo Natsuhara, *[a] Ryogo Saito,[a] Hiroka Aonuma,[b] Tatsuya Sakurai,[c] Shunya Okamoto,[a] Moeto Nagai, [a] Hirotaka Kanuka[bc] and Takayuki Shibata*[a]

Received 14th September 2021,
Accepted 15th November 2021

DOI: 10.1039/d1lc00829c

rsc.li/loc

In this study, we introduce polydimethylsiloxane (PDMS)-based microfluidic devices capable of sequential dispensing of samples into multiple reaction microchambers in a single operation to provide a fast and easy sample-to-answer platform for multiplexed genetic diagnosis of multiple viral infectious diseases. This approach utilizes the loop-mediated isothermal amplification (LAMP) method to amplify and detect specific nucleic acid (DNA/RNA) targets. We present a microfluidic flow control theory for sequential liquid dispensing phenomena, which provides design guidelines for device optimization. The device specifications, such as the possible dispensing number and maximal allowable flow rate, can be theoretically designed by optimizing the geometric dimensions of the microchannels and a pair of passive stop valves integrated into each microchamber together with the water contact angles of the materials used to fabricate the microfluidic devices. In addition, a passive stop valve with a vertical-type phaseguide structure was designed to improve device performance. We could simultaneously diagnose coronavirus disease 2019 (COVID-19) and other infectious diseases, such as severe acute respiratory syndrome (SARS), seasonal influenza A, and pandemic influenza A (H1N1) 2009. The colorimetric reverse transcription LAMP (RT-LAMP) assay suggests that the four viral infectious diseases can be detected within 30 min using a hue-based quantitative analysis, and the naked eye using our microfluidic devices.

Introduction

Coronavirus disease 2019 (COVID-19), caused by the severe acute respiratory syndrome coronavirus 2 (SARS-CoV-2), is a highly infectious disease that has rapidly spread worldwide after the first cases were registered in Wuhan, China, in late December 2019.[1–5] The COVID-19 pandemic has caused unprecedented disruptions in healthcare, economic, and social systems, presenting a treacherous situation that threatens people's lives, livelihoods, and well-being. To prevent the spread of COVID-19, timely and accurate diagnostic testing for SARS-CoV-2 is a crucial first step in enabling active surveillance, early detection, and outbreak management.

At present, three different types of tests are available for COVID-19: 1) molecular tests, 2) antigen tests, and 3) antibody tests.[6–10] Both molecular and antigen tests can be categorized as diagnostic tests that identify an active COVID-19 infection, whereas antibody tests (also referred to as serological tests) can be used to detect a past infection. Among these tests, the real-time reverse transcription polymerase chain reaction (RT-qPCR) test is a gold standard test for diagnosing COVID-19 owing to its advantages, such as high sensitivity, accuracy, and reliability.[6,10] However, the requirements for expensive instrumentation and uniquely trained personnel have limited its practical applications to point-of-care testing (POCT).[11]

The recent advent of clustered regularly interspaced short palindromic repeats (CRISPR)-based technology has made a rapid molecular diagnostics platform for COVID-19 possible with a sensitivity and specificity comparable to those of RT-qPCR.[12,13] Paper-strip-based rapid antigen tests for COVID-19 offer advantages such as shorter turnaround times (up to 30 min) and reduced costs; however, they are inherently less sensitive because they detect specific viral proteins rather than amplified nucleic acids.[6,7] In contrast, paper-strip-based rapid antibody tests detect immunoglobulin M (IgM) and IgG antibodies directed against SARS-CoV-2 within 15–20 min. The lateral flow immunoassay technology, utilized by these tests, is acceptable as a POCT platform for COVID-19 owing

[a] *Department of Mechanical Engineering, Toyohashi University of Technology, Aichi 441-8560, Japan. E-mail: d-natsuhara@mems.me.tut.ac.jp, shibata@me.tut.ac.jp*
[b] *Department of Tropical Medicine, The Jikei University School of Medicine, Tokyo, 105-8461, Japan*
[c] *Laboratory Animal Facilities, The Jikei University School of Medicine, Tokyo, 105-8461, Japan*

† Electronic supplementary information (ESI) available. See DOI: 10.1039/d1lc00829c

to its advantages such as ease of use, affordability, and relatively high sensitivity and reliability. Although antibody testing cannot be used for diagnosing COVID-19, it can be used as an important complementary approach to RT-qPCR to detect and manage COVID-19 owing to a delayed immune response to the virus.[7,9]

Loop-mediated isothermal amplification (LAMP) is a promising candidate POCT platform, which is employed as an alternative method for field-deployable viral diagnostics based on nucleic acid sequence-based amplification.[14,15] The LAMP assay is one of the most commonly used isothermal nucleic acid amplification techniques in which a few copies of specific nucleic acid (DNA/RNA) targets can be amplified approximately 10^9 times within 30–60 min under isothermal conditions (60–65 °C), using a set of 4–6 particularly designed LAMP primers. Therefore, this technique only requires a simple hot-water bath instead of expensive instrumentation, such as a thermocycler, for a precise temperature control and rapid thermal cycling in PCR. Moreover, simple naked-eye colorimetric detection is possible using various indicator dyes.[16] For example, pH-sensitive indicator dyes, such as phenol red, are used to monitor significant pH changes from alkaline to acidic environments associated with the LAMP reaction, whereas metal-ion indicator dyes (*e.g.*, hydroxynaphthol blue) are used to monitor a rapid decrease in the concentration of free Mg^{2+} ions owing to the formation of insoluble magnesium pyrophosphate during DNA amplification. In addition, many recent studies have claimed that the diagnostic sensitivity and specificity of the reverse transcription LAMP (RT-LAMP) for detecting SARS-CoV-2 viral RNA was comparable to that of the RT-qPCR method.[17–22] Thus, the LAMP method has considerable potential for providing a cost-effective and easy-to-use diagnostic tool and for enabling on-site diagnoses with little equipment. However, technological issues persist in the LAMP assay. The most effective strategy to realize the eventual control of the COVID-19 pandemic is to provide a platform for enabling an early and accurate detection of multiple simultaneous viral infections. That is, identification of SARS-CoV-2 variants, and simultaneous diagnosis of COVID-19 and other infectious diseases, such as influenza viruses A and B. In the conventional LAMP assay, it is necessary to prepare and individually test many sample/reagent mixtures for each target infectious virus. Therefore, diagnosis of multiple viral diseases requires laborious operations and a relatively large amount of LAMP reagents (in general, 10–25 μL for testing a single virus), resulting in higher cost and longer time required to provide a test result.

To address this issue, the lab-on-a-chip technology is being harnessed to enable multiplexed LAMP assays in microfluidic devices for the simultaneous detection of targeted nucleic acids (DNA or RNA) in a single reaction. A centrifugal microfluidic lab-on-a-disc (LOD) allows automated operation for multiplexed genetic diagnosis, including pumping, sample mixing, timed valving, flow switching, volume metering, and sequential loading to multiple reaction chambers, by precise control of the interplay of centrifugal and capillary forces, followed by real-time monitoring of DNA amplification reactions during the LAMP assay.[23–26] For example, simultaneous detection of ten types of pathogenic bacteria in aquatic animals within 30 min (ref. 23) and four types of foodborne pathogens within 65 min (ref. 24) was successfully demonstrated in LOD devices. As another microfluidic platform, stationary chamber-based microfluidic devices integrated with multiple reaction chambers also have the potential for multiplexed diagnosis and genotyping of pathogens, such as bacteria and viruses.[27–30] For example, simultaneous detection (within 30 min) of five types of pathogens that cause equine respiratory infections[29] and six types of respiratory viruses such as influenza A, B, and human adenovirus, within 60 min (ref. 30) were successfully performed in microfluidic devices. Nevertheless, both diagnostic platforms require complex and expensive instrumentation, and/or laborious and multiple operations.

For an early detection of infectious disease events, we have developed a multiplexed genetic diagnostic device capable of sequential dispensing of samples into an array of reaction microchambers to achieve a rapid and simple identification of multiple infectious viruses in a single operation by combining the microfluidic technology and LAMP method. In our previous study,[31] we fabricated diagnostic devices to detect a DNA-based plant virus infecting tomato. In addition, we could simultaneously detect four types of RNA-based plant viruses within 60 min using the RT-LAMP method that infected cucurbits. In addition, we detected a toxic plant (*C. autumnale*-specific DNA regions) using the microfluidic diagnostic device within 60 min, providing a reliable screening method for plant poisoning in emergency medical care situations.[32] In this study, we propose a microfluidic flow control theory for sequential dispensing of samples into multiple chambers, which helps clarify the design guidelines for the optimization of microfluidic devices. Moreover, we can simultaneously diagnose COVID-19 and other infectious diseases, such as severe acute respiratory syndrome (SARS), seasonal influenza A, and pandemic influenza A (H1N1) 2009.

Materials and methods

Fabrication process of the multiplexed diagnostic device

Polydimethylsiloxane (PDMS)-based microfluidic devices were fabricated using a modified soft lithography process with a thick negative photoresist (SU-8 3050, MicroChem Corp., Newton, MA, USA) as a mold. Fig. 1a shows that the fabricated devices consisted of two main parts: a mixing region and a dispensing region (also used as the reaction and detection regions). The width and height of the microchannel were approximately 200 and 50 μm, respectively. To create deep localized microchamber structures (diameter = 2 mm; depth = 1 mm), hemispherical polymer beads (diameter = 2 mm; supplied by SAYAKOBO, Yokohama, Japan) were glued at a center position on the top surface of each SU-8 chamber

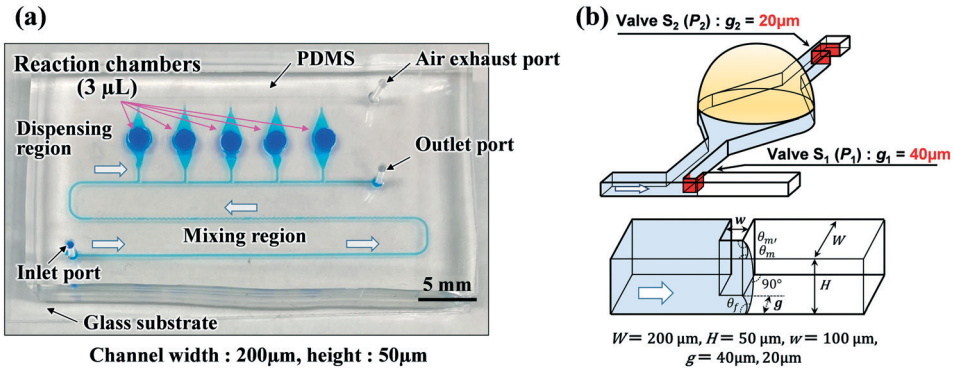

Fig. 1 Schematic of the microfluidic diagnostic device capable of sequential sample dispensing for multiplexed genetic diagnosis. (a) The fabricated PDMS microfluidic device consisting of an array of five reaction microchambers (volume of each ≈3 μL) was filled with blue-colored water. (b) Detailed design of the reaction microchamber integrated with a pair of designed vertical-type phaseguide structures, which can be fabricated using a one-step photolithography approach.

pattern using an epoxy adhesive (Araldite, Huntsman Japan, Kobe, Japan) at room temperature for 12 h. SU-8 master mold was replicated in PDMS (Silpot 184, Dow Corning Toray Co., Ltd., Tokyo, Japan) after curing at 80 °C for 40 min on a hot plate (EC1200-N, AS ONE, Osaka, Japan). Finally, after peeling the PDMS off the SU-8 master mold, circular holes (diameter = 1.0 mm) for the inlet and outlet ports were punched into the fabricated PDMS microfluidic devices using a biopsy punch piercing tool (Kai Industries Co. Ltd., Gifu, Japan). The fabrication process of the microfluidic diagnostic devices was thoroughly described in our previous study report.[31] The size of fabricated microfluidic devices was approximately 45 mm × 25 mm, as shown in Fig. 1a.

Vertical-type phaseguide structure as a passive valve

In our previous study,[31] we demonstrated sequential sample dispensing into five microchambers (volume ≈3 μL) by controlling the burst pressures in three types of phaseguide ridge structures (hereinafter referred to as lateral-type phaseguides[33,34]) with different inclined angles against the flow direction, as presented in Fig. S1.† In this study, we designed a vertical-type phaseguide structure as a passive stop valve to improve the valve performance. Fig. 1b illustrates a pair of passive stop valves that was integrated into each microchamber, in which phaseguides S_1 (designed with burst pressure P_1) and S_2 (designed with burst pressure P_2) acted as temporary and permanent stop valves, respectively. The valve S_2 also helped exhaust the air in microchambers. This simple geometric design allows the use of a one-step photolithography process, thereby reducing the processing time (~1 h), whereas a complicated two-step photolithography process (~3 h) was required for the fabrication of the lateral-type phaseguides. Moreover, the burst pressure can be controlled using the gap distance (g) between the vertical sidewalls of the phaseguide and microchannel. This improves the dimensional accuracy and reproducibility of the phaseguide structures because the lateral dimensions are consistently better accuracy than the vertical ones in the photolithography process. In addition, the pressure differences between each phaseguide (P_1 *vs.* P_2) can be improved, and a higher burst pressure (P_2) for the permanent stop valve S_2 can be designed while maintaining a relatively low burst pressure (P_1) for the temporary stop valve S_1. The ESI† section provides a comparison between the performance of the-lateral and vertical phaseguides (see Tables S1 and S2†).

In summary, the dispensing procedure was as follows: first, the flow of water was stopped after reaching the temporary stop valve S_1 (burst pressure P_1), and the flow direction was subsequently changed toward the microchamber. After the microchamber was filled with water, the flow of water was stopped at the permanent stop valve S_2 (burst pressure P_2), and then the flow toward the second microchamber occurred by passing through valve S_1 because $P_1 < P_2$. The process is repeated to sequentially fill all microchambers with water at a high repeatability and reproducibility rate.

Operating procedure for the colorimetric LAMP assay

The operating procedure for the multiplexed LAMP assay in microfluidic diagnostic devices for simultaneous detection of RNA-based coronaviruses (SARS-CoV-2 and SARS-CoV) and influenza viruses (seasonal influenza A and pandemic influenza A (H1N1) 2009, also referred to as A (H1N1) pdm09) is as follows: first, four types of specific primer sets (volume range, 0.6–1.8 μL), expected to amplify viral RNA attributable to the targeted infectious diseases, were pre-spotted and dried in each reaction chamber (volume ≈3 μL) on a hot plate at 80 °C for 5 min. Subsequently, both the microchambers and microchannels were sealed with a glass substrate (S9213, Matsunami Glass Ind., Ltd., Osaka, Japan) using a silicone-based adhesive transfer tape (91022, 3M, St. Paul, MN, USA). After dispensing the sample mixture (viral RNA or cDNAs derived from viral RNA targets) and LAMP reagents into five reaction chambers at a flow rate of 10 μL min^{-1} using a syringe pump (YSP-201; YMC Co., Ltd., Kyoto,

Japan), the inlet and outlet ports were sealed with a glass wafer using a silicone-based adhesive double-sided tape (No. 5303W, Nitto Denko Corp., Osaka, Japan). The microfluidic device was further mechanically clipped to prevent leakage at the glass/PDMS/glass interface, and then immersed in a hot water bath (TB-1NC, AS ONE, Osaka, Japan) to amplify the targeted nucleic acids (RNA or cDNA) through the RT-LAMP reaction, respectively, under isothermal conditions at 58 °C for 30–60 min. Hydroxy naphthol blue (HNB; purchased from FUJIFILM Wako Pure Chemical Corp., Osaka, Japan) was used as an indicator for visible colorimetric detection of the RT-LAMP reaction using a smartphone for the hue-based quantitative analysis together with a rapid and easy naked-eye detection. The final concentration of HNB was adjusted to 120 μM in a mixture of the sample and LAMP reagents in each reaction chamber (volume ≈3 μL). Commercially available RT-LAMP-based diagnostic kits containing the primer sets and positive control templates (cDNAs derived from viral RNA targets) for the detection of three types of viruses (SARS-CoV, influenza A, and A (H1N1) pdm09) were purchased from Eiken Chemical Co., Ltd. (Tokyo, Japan). In contrast, we particularly designed a primer set for the detection of SARS-CoV-2 (unpublished data; The Jikei University School of Medicine, Tokyo, Japan). In addition, SARS-CoV-2 viral RNA (JPN/AI/I-004), provided by Dr. Masayuki Saijo (National Institute of Infectious Diseases, Japan) as a positive control for the COVID-19 diagnoses, was used for diagnostic testing in the microfluidic device. The Loopamp® RNA amplification kit (Eiken Chemical Co., Ltd.) was employed to perform the RT-LAMP reactions, which mainly contained the 2× reaction mix and enzyme mix (a mixture of *Bst* DNA polymerase and AMV reverse transcriptase). The primer set (volume = 0.6 μL) was pre-spotted and dried in a reaction chamber to detect SARS-CoV-2, according to our optimized RT-LAMP reaction conditions. In contrast, the required volumes of the other primer sets (1.5 μL for SARS-CoV, 1.8 μL for influenza A and A (H1N1) pdm09) were determined according to their protocols recommended by Eiken Chemical Co., Ltd. (Tokyo, Japan).

Results and discussions

Microfluidic flow control theory for sequential dispensing

An optimal design theory for the burst pressure of the permanent stop valve S_2. For the design and optimization of our microfluidic diagnostic devices, at least two questions must be answered: 1) how many microchambers can be dispensed?, and 2) how fast can a sample-reagent mixture be introduced into the diagnostic device? Fig. 2 shows a typical experimental result, which demonstrates that a liquid is sequentially dispensed into an array of ten microchambers (each volume ≈3 μL) in a single-row format, where water colored with blue food color (0.1% w/v) was introduced into a microchannel (W = 190.6 μm, H = 51.4 μm) with a syringe pump at a flow rate of 10 μL min^{-1}. Contrary to our expectations, after the sixth microchamber was filled with water, the flow of water passed through the permanent stop valve S_2 of the first chamber, as shown in Video S1.† In the experiments under different flow rate conditions, once the overflow problem occurred, water was not dispensed into any more chambers. In addition, stop valve S_2 of the first chamber overflowed first. The results indicated that valve S_2 of the first chamber was constantly exposed to the highest hydrostatic pressure. Therefore, we estimated the required burst pressure P_2 for the first chamber by deriving an equation as follows:

$$P_2 > P_1 + (m-1)\Delta P(L_1) + \Delta P(L_2) + \Delta P(L_3) \quad (1)$$

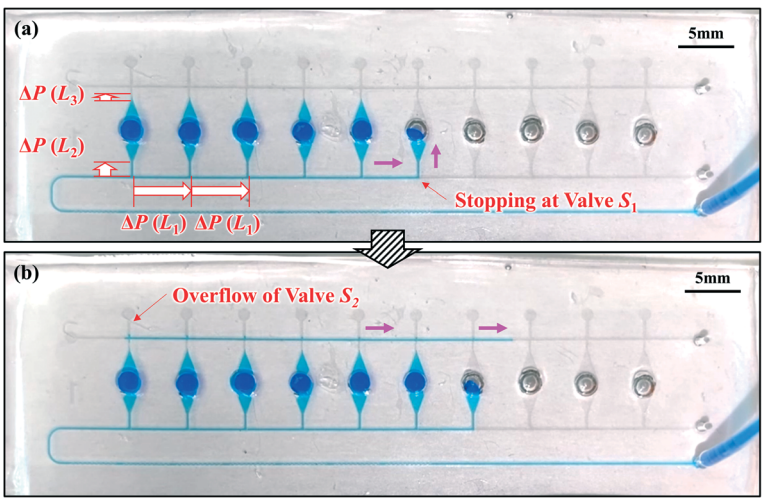

Fig. 2 Experimental results showing sequential liquid dispensing into the microchambers placed in a single row (L_1 = 5.0 mm) at a flow rate of 10 μL min^{-1}. The burst pressures of the temporary stop valve S_1 (g = 36.5 μm) and permanent stop valve S_2 (g = 17.9 μm) were designed to be P_1 = 3.23 and P_2 = 5.95 kPa, respectively. (a) The flow direction was changed toward the sixth microchamber after reaching the temporary stop valve S_1, and subsequently the microchamber was filled with the blue-colored water. (b) Water flew out of the permanent stop valve S_2 of the first microchamber after the sixth microchamber was filled with water.

Table 1 Comparison between N_{th} and N_{ex} of the microchambers that could be dispensed, for microfluidic devices in the one-row format (L_1 = 5.0 mm, L_2 = 1.25 mm, and L_3 = 0.2 mm) and in the staggered two-row format (L_1 = 2.5 mm, L_2 = 1.0 mm, and L_3 = 0.2 mm) as a function of the flow rate. N_{ex} represents the mean ± standard deviation values computed over ten experiment replicates

	Single-row format (L_1 = 5.0 mm)		Two-row format (L_1 = 2.5 mm)	
Flow rate (μL min^{-1})	Theoretical number (N_{th})	Experimental results (N_{ex})	Theoretical number (N_{th})	Experimental results (N_{ex})
5.0	10	9.8 ± 0.4	10	10.0 ± 0.0
7.5	8	7.8 ± 0.6	—	—
10	6	6.1 ± 0.7	10	9.5 ± 1.0
15	4	4.7 ± 0.8	8	7.4 ± 1.0
20	3	4.2 ± 0.4	6	6.4 ± 1.1
30	—	—	4	4.5 ± 0.5

where P_1 is the burst pressure of the temporary stop valve S_1 of the first chamber; $\Delta P(L_1)$, $\Delta P(L_2)$, and $\Delta P(L_3)$ are the pressure differences required to flow a liquid in a microchannel with lengths L_1, L_2, and L_3, respectively; and, m is the number of microchambers that had been filled completely with water. The microchannel lengths (L_1, L_2, and L_3) are defined as shown in Fig. 2. L_1 is the distance between each microchamber. L_2 and L_3 are distances from the microchannel T-junction to the microchamber inlet and from the microchamber outlet to the permanent stop valve (S_2), respectively. Here, the flow resistance inside the microchamber is not considered because of its considerably larger space (both width and depth) than that of the narrow microchannels. The theoretical pressure drop $\Delta P(L)$ in a rectangular microchannel (width W, height H, and length L) is described as follows:[33]

$$\Delta P(L) = Q \times \frac{12\eta L}{H^3 W}\left(1 - 0.630\frac{H}{W}\right)^{-1} \quad (2)$$

where η is the dynamic viscosity of the liquid (η = 1 mPa s for water), and Q is the volumetric flow rate.

In addition, the burst pressure of the vertical-type phaseguide, $P(g)$ (Pa), can be derived as follows:

$$P(g) = -\gamma\left(\frac{\cos(\min(\theta_m + 90°, 180°)) + \cos\theta_m}{g} + \frac{\cos\theta_m + \cos\theta_f}{H}\right) \quad (3)$$

where g is the gap between the vertical sidewalls of phaseguide and microchannel, H is the height of the rectangular microchannel, θ_m is the water contact angle for the surfaces of the top and sidewalls of the microchannel at a narrow gap (*i.e.*, PDMS), and θ_f is the water contact angle for the bottom surface of the microchannel (*i.e.*, the silicone-based adhesive tape). The angle θ_m + 90° (≤180°), in the first term on the right side of eqn (3) is defined as the water contact angle at the back edge of the vertical-type phaseguide structure. The resulting burst pressures (corresponding to Fig. 2) were P_1 = 3.23 and P_2 = 5.95 kPa, for the temporary stop valve S_1 (g = 36.5 μm) and permanent stop valve S_2 (g = 17.9 μm and W = 93.6 μm), respectively. In addition, the surface tension of water was 0.073 N m^{-1},[34] and the water contact angles θ_m and θ_f were 108 and 97°, respectively.

According to eqn (1) and (2), the number of chambers that can be dispensed (defined as the theoretical dispensing number, N_{th}) decreases with an increasing flow rate Q owing to an increase in the pressure drop $\Delta P(L)$ while the liquid flows in the microchannel. Table 1 (2nd and 3rd columns from the left) compares the theoretical (N_{th}) and experimental (N_{ex}) numbers of microchambers that could be dispensed for microfluidic devices in a single-row format (L_1 = 5.0 mm, L_2 = 1.25 mm, and L_3 = 0.2 mm), as a function of the flow rate. Eqn (2) was used to calculate $\Delta P(L_1)$, $\Delta P(L_2)$, and $\Delta P(L_3)$ at a flow rate of 10 μL min^{-1} that were 0.465, 0.116, and 0.048 kPa, respectively. Each experimental dispensing number (N_{ex}) represents the mean ± standard deviation of ten experimental replicates. As predicted using the proposed dispensing theory, the N_{ex} values satisfactorily agreed with the N_{th} values for flow rates in the range of 5.0–20 μL min^{-1}. Table S3† lists the theoretical values calculated at different flow rates.

To realize efficient operation for diagnostics, the maximal possible flow rate should be increased to reduce the time required to dispense a sample-reagent mixture into a device. According to the proposed dispensing theory, reducing the microchannel length, in particular L_1, increases the flow rate for the same dispensing number. That is, for the same flow rate, decreasing L_1 will increase the maximal possible dispensing number. Therefore, a novel microchamber array was designed to offer a shorter microchannel length (L_1 = 2.5 mm), as shown in Fig. 3. As predicted by the theoretical model, the device designed in the staggered two-row format allowed successful dispensing into all ten microchambers, even at a flow rate of 10 μL min^{-1}, as shown in Video S2,† compared with dispensing into only six chambers, as was the case for the single-row format device (L_1 = 5.0 mm) (Fig. 2). First and second columns from the right of Table 1 demonstrate that N_{th} and N_{ex} agreed reasonably at flow rates in the range of 5.0–30 μL min^{-1}. The theoretical values calculated at different flow rates are listed in Table S4.†

Fig. 4a presents a typical example of a liquid–air meniscus pinned on the back edge of the vertical-type phaseguide (S_1) with a sharp corner radius (r = 8 μm) of a convex structure. Under the optimal photolithography conditions in our experiments, the corner radius was maintained at approximately 8 μm. In contrast, when the corner radius at

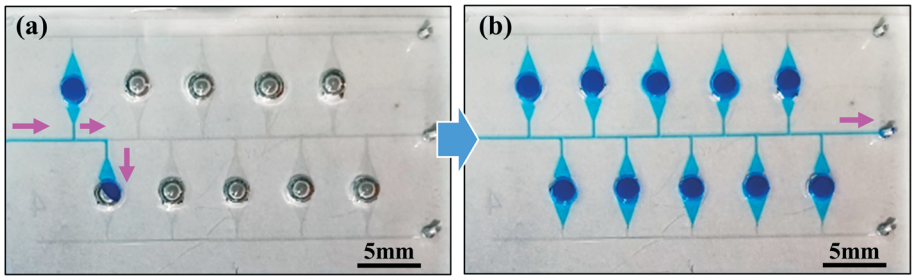

Fig. 3 Experimental results showing sequential liquid dispensing into the microchambers placed in the staggered two-row format (L_1 = 2.5 mm) at a flow rate of 10 μL min^{-1}. The burst pressures of S_1 (g = 36.5 μm) and S_2 (g = 17.9 μm) were designed to be P_1 = 3.23 and P_2 = 5.95 kPa, respectively. (a) The flow toward the second microchamber occurred by passing through the temporary stop valve S_1 of the first microchamber immediately after reaching the permanent stop valve S_2 of the first microchamber. (b) All microchambers were sequentially filled with water by repeating this process.

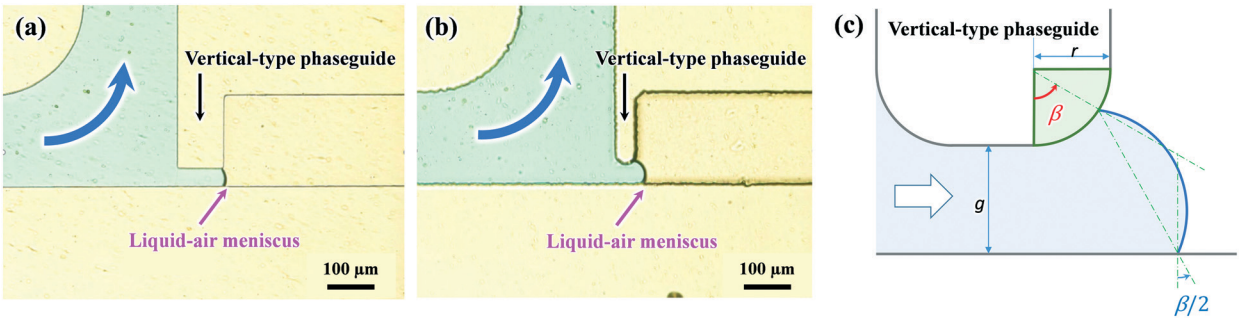

Fig. 4 Optical microscopy images showing the liquid–air meniscus being pinned on the back edge of the vertical-type phaseguide S_1 with a corner radius of (a) 8 μm, and (b) 25 μm. (c) Theoretical model for describing the burst pressure considering the corner radius of S_1.

the back edge of the phaseguide structure was relatively large (r = 25 μm, as shown in Fig. 4b), the front of the meniscus advanced further along the sidewall of the microchannel rather than at the position of angle (β), corresponding to being pinned at the corner of the phaseguide. The angle β is defined in Fig. 4c. In this case, the meniscus was inclined perpendicular to the sidewall at an angle of $\beta/2$. Thus, when the corner radius r at the back edge of the phaseguide structure is not negligible, the theoretical burst pressure is expressed as follows:

$$P(g, r, \beta) = -\gamma\left(\frac{\cos(\min(\theta_m + \beta, 180°)) + \cos\theta_m}{g + r(1 - \cos\beta)} + \frac{\cos\theta_m + \cos\theta_f}{H}\right) \quad (4)$$

where the denominator, $g + r\,(1 - \cos\beta)$, on the first term is the redefined gap distance g' between the position corresponding to being pinned at the corner of the phaseguide and vertical sidewall of the microchannel, as shown in Fig. S2.†

The burst pressure decreased to approximately 90% at r/g = 0.20 compared with that of the ideal burst pressure (r = 0 μm). Considering the dimensional accuracy of negative thick photoresist (SU-8) patterns in a typical photolithography process, it is desirable to maintain the corner radius of the phaseguide below at least the ratio r/g = 0.40, resulting in an ideal burst pressure of 85% or higher. The influence of the corner radius of the phaseguide structure on the theoretical burst pressure is thoroughly described in Fig. S3.†

An optimal design theory for the burst pressure of the temporary stop valve S_1. As described earlier, the possible dispensing number and maximal flow rate can be determined using the proposed dispensing theory. However, the minimum possible size of the burst pressure P_1 for designing the temporary stop valve S_1 should be determined to achieve an optimized design for our diagnostic microfluidic devices. According to eqn (1), reducing the burst pressure increases the dispensing number and flow rate. Therefore, the influence of gap distance of the temporary stop valve S_1 on the dispensing behavior was investigated.

Fig. 5a illustrates an example of sequential liquid dispensing into an array of ten microchambers in the staggered two-row format, with a gap distance of g = 122.8 μm for valve S_1 (W = 199.1 μm, H = 54.4 μm). Furthermore, dispensing was performed at a flow rate of 10 μL min^{-1}, and the estimated burst pressure was P_1 = 1.36 kPa. Before the fifth microchamber was completely filled, the flow toward the sixth microchamber occurred by passing through valve S_1 of the fifth chamber. Fig. 5b shows that the flow of water stopped after reaching the entrance of the microchamber. This unfavorable result could be attributed to the meniscus

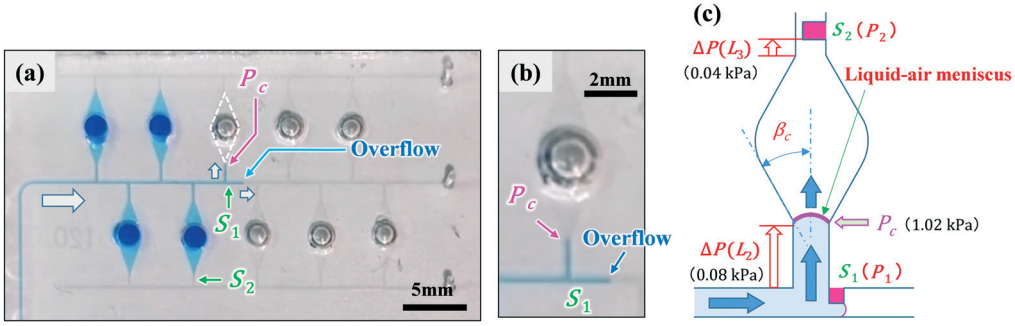

Fig. 5 Experimental result showing the influence of the burst pressure P_1 of the temporary stop valve S_1 on the performance of sequential liquid dispensing. (a) An example of sequential liquid dispensing into an array of ten microchambers in the staggered two-row format, at a gap of 122.8 μm of valve S_1 (P_1 = 1.36 kPa, W = 199.1 μm, H = 54.4 μm) at a flow rate of 10 μL min^{-1}. (b) Close-up view demonstrating stopped water flow after reaching the entrance of the microchamber, while the flow toward the next chamber occurred by passing through S_1. (c) Theoretical model for the design optimization of S_1.

pinning effect at this position owing to the sudden expansion of the microchannel, as illustrated in Fig. 5c. The burst pressure P_c induced at the entrance of the microchamber is described as

$$P_C = -\gamma\left(\frac{2\cos(\min(\theta_m+\beta_c,180°))}{W+2r_c(1-\cos\theta)}+\frac{\cos\theta_m+\cos\theta_f}{H}\right)\quad(\beta\le\beta_c) \tag{5}$$

where β is the angle of a certain position corresponding to being pinned on the rounded corner (corner radius is indicated by r_c) at the intersection of the microchannel and entrance of the microchamber. However, β must be less than β_c, which is the angle of the intersection of the microchannel and microchamber. Definitions of these parameters are presented in Fig. 5c. In this experiment, the estimated burst pressure P_c was 1.02 kPa, for r_c = 39.4 μm and β_c = 19.9°. Here, although the calculated burst pressure P_c exhibited a maximum of 1.18 kPa at β = 56° according to eqn (5), the resulting P_c was determined considering the constraint $\beta \le \beta_c$. We derived a relationship to estimate the required burst pressure P_1 of each chamber as follows:

$$P_1 > \Delta P(L_2) + P_C + \Delta P(L_3) \tag{6}$$

This relationship was derived by assuming that the burst pressure P_1 must be higher than the total pressure required to introduce the liquid until it reaches valve S_2 (g = 28.3 μm and W = 102.0 μm) to fill the microchamber. However, it should be noted that the third term on the right side, $\Delta P(L_3)$, is not always required to fill the microchamber.

The influence of the theoretical burst pressure P_1 of the temporary stop valve S_1 on the performance of sequential liquid dispensing is summarized in Table 2. Ten experiments were performed under the same conditions on microfluidic devices in the staggered two-row format (L_1 = 2.5 mm, L_2 = 1.00 mm, and L_3 = 0.2 mm). The flow of water was successfully stopped at valve S_1 for all devices with the burst pressures of P_1 = 2.69 and 1.70 kPa (g = 45.3 and 85.0 μm, respectively) at flow rates in the range of 5.0–15 μL min^{-1}. According to eqn (6), this favorable result is achieved because both the theoretical burst pressures P_1 were approximately 1.5 times greater than the theoretical total pressure, $\Delta P(L_2)$ + P_c + $\Delta P(L_3)$. In contrast, the flow of water always passed through valve S_1 before filling the microchamber when the burst pressures dropped to P_1 = 1.36 and 1.17 kPa (g = 122.8 and 162.1 μm, respectively) at flow rates in the range of 2.5–10 μL min^{-1} (Fig. 5). In particular, the theoretical burst pressure P_1 was still higher than the theoretical total pressure calculated using eqn (6), which was probably caused by the fact that the interface between the top surface of the vertical phaseguide and the adhesive tape was not completely sealed, resulting in a decrease in the actual burst pressure compared

Table 2 Influence of the theoretical burst pressure P_1 of S_1 on the performance of sequential liquid dispensing. The words 'Succeeded' and 'Failed' represent two different dispensing behaviors where the flow of water was stopped at S_1 and passed through S_1, respectively. The theoretical total pressure is $\Delta P(L_2)$ + P_c + $\Delta P(L_3)$ for the microfluidic devices in the staggered two-row format (L_2 = 1.00 mm, L_3 = 0.2 mm, r_c = 39.4 μm, and β_c = 19.9°) as a function of the flow rate

Gap distance	Burst pressure	Flow rate (μL min^{-1})			
g (μm)	P_1 (kPa)	2.5	5.0	10	15
45.3	2.69	—	Succeeded	Succeeded	Succeeded
85.0	1.70	—	Succeeded	Succeeded	Succeeded
122.8	1.36	Failed	Failed	Failed	—
162.1	1.17	Failed	Failed	Failed	—
Theoretical total pressure (kPa)		1.05	1.07	1.13	1.19

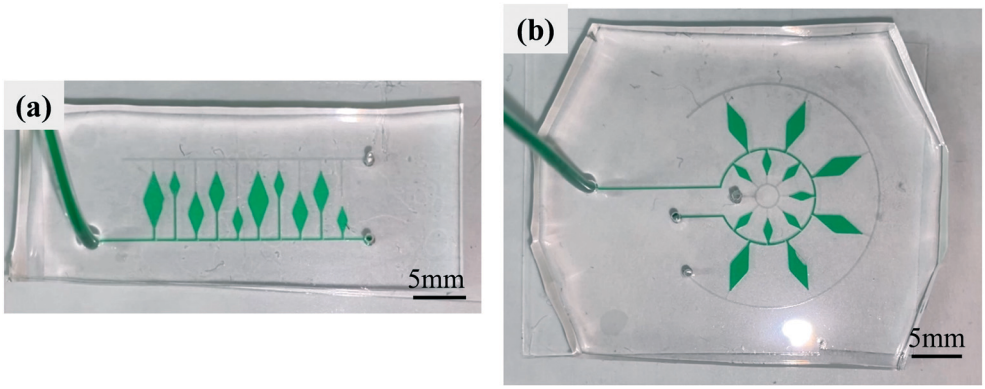

Fig. 6 Experimental results showing sequential liquid dispensing into an array of microchambers. For visualization, the green-colored water was introduced into the devices, at a flow rate of 10 μL min^{-1}. (a) A microfluidic device with ten microchambers and three different sizes at different locations away from the main microchannel. (b) A microfluidic device with thirteen microchambers at two different sizes arranged in two rows on the circumference.

with the theoretical one. Here, the estimated values of $\Delta P(L_2)$ and $\Delta P(L_3)$ were in the ranges of 0.019–0.113 and 0.009–0.055 kPa, respectively, at flow rates in the range of 2.5–15 μL min^{-1}, in a microchannel (W = 199.1 μm and H = 54.4 μm). Moreover, these values are considerably smaller than P_c = 1.02 kPa (r_c = 39.4 μm and β_c = 19.9°) induced at the entrance to the microchamber. Therefore, the burst pressure P_1 must be designed to be sufficiently large with respect to the pressure barrier P_c.

Thus, according to eqn (1)–(6), the device specifications, such as the possible dispensing number and maximal allowable flow rate, can be theoretically designed by optimizing the geometric dimensions of the microchannels and a pair of passive stop valves integrated into each microchamber together with the water contact angles of the materials used to fabricate the microfluidic devices.

In addition, the developed dispensing method enabled a microfluidic device a high design flexibility. Fig. 6a presents an example of a microfluidic device with sequential liquid dispensing into an array of microchambers with three different sizes at different locations away from the main microchannel, where water colored with a green food coloring (0.1% w/v) was successfully introduced into all ten microchambers at a flow rate of 10 μL min^{-1}, as shown in Video S3.† Another example is shown in Fig. 6b, where microchambers of two different sizes were arranged in two rows on the circumference. Even with such a complicated arrangement, the green-colored water was successfully dispensed sequentially into all 13 microchambers at a flow rate of 10 μL min^{-1}, as shown in Video S4.† Yamada and Seki[35] proposed a method for dispensing, transporting, and mixing a number of nanoliter-sized droplets simultaneously in microfluidic devices using hydrophobic passive valves; however, it required the precision alignment and bonding of two PDMS microchannels, which is not appropriate for our application. As another typical method for liquid dispensing into multiple microchambers,[36] a strict design constraint exists in which an array of microchambers and a microchannel forming a network are symmetrically arranged owing to the pressure drop equalization in each flow path from the inlet to the outlet port. In contrast, our simple and sequential liquid dispensing method provides substantial flexibility in the design of microfluidic devices. Another advantage for our developed method is that there is no need to let the liquid flow out from the outlet side of the microchamber to be filled. In our diagnostic applications, this feature can prevent LAMP primers that had been pre-spotted in the microchambers from flowing out.

Multiplexed LAMP assay for the diagnosis of human viral diseases

We explored the possibility of rapid simultaneous diagnosis of multiple viral infections using the fabricated microfluidic devices. Fig. 7a shows the experimental results for the detection of SARS-CoV-2 viral RNA (the cause of COVID-19) using the colorimetric RT-LAMP method on the microfluidic device. Four types of specific primer sets for the detection of SARS-CoV-2, SARS-CoV, seasonal influenza A virus, and the influenza A (H1N1) pdm09 virus were pre-spotted and dried in reaction chambers 2, 3, 4, and 5, respectively, while no primers were pre-spotted in reaction chamber 1, as a negative control. The SARS-CoV-2 viral RNA was mixed with the LAMP reagents at a concentration of 200 copies per μL, and subsequently introduced into the device at a flow rate of 10 μL min^{-1}. The RT-LAMP assay was conducted at 58 °C for 60 min in a hot water bath. As expected, a positive reaction, manifested by a color change of HNB in the LAMP reaction solution from violet to sky blue, was clearly observed only in chamber 2. Similarly, the cDNA samples of different types, derived from the viral RNA targets causing SARS, seasonal influenza A, and influenza A (H1N1) pdm09 were introduced into each device, followed by the LAMP assays at 58 °C for 60 min, as shown in Fig. 7b–d. A positive reaction for enabling the detection of SARS-CoV, seasonal influenza A, and influenza A (H1N1) pdm09 occurred without any cross-

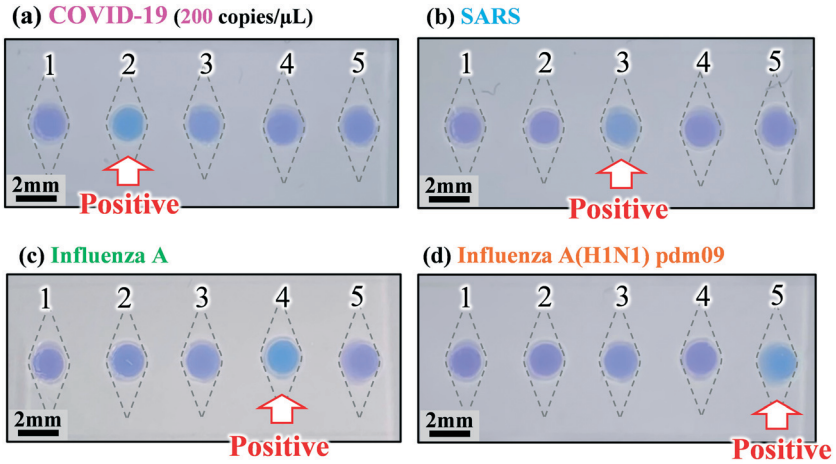

Fig. 7 Photographs taken with a smartphone camera, showing the colorimetric RT-LAMP detection of (a) SARS-CoV-2 viral RNA causing COVID-19 disease, and the LAMP detection of cDNA samples of viral RNA targets causing (b) SARS, (c) seasonal influenza A, and (d) influenza A (H1N1) pdm09, after heating at 58 °C for 60 min. Four types of specific primer sets for the detection of SARS-CoV-2, SARS-CoV, seasonal influenza A, and influenza A (H1N1) pdm09 were dried in reaction chambers 2, 3, 4, and 5, respectively, while no pre-spotted primers in reaction chamber 1 is a negative control.

contamination in chambers 3, 4, and 5, respectively. Moreover, a color change from violet to sky blue in each positive chamber was clearly observed by the naked eye after the LAMP assays were conducted for 30 min.

Quantitative evaluations of color differences between a positive reaction (sky blue) and a negative reaction (violet) were conducted for each microchamber, based on a representation of the CIE $L^*a^*b^*$ color space (CIELAB), which is a widely used three-dimensional (3D) color spaces defined by the International Commission on Illumination (CIE) in 1976.[37] The CIELAB color space is more accurate when considering human-perceived color differences. In this color space, L^* indicates lightness, and a^* and b^* are chromaticity coordinates. First, the RGB values for each microchamber were quantified using the ImageJ software package (version 1.52a, National Institutes of Health, USA), and subsequently converted to *XYZ* tristimulus values in the CIE *XYZ* color space. Next, the color parameter values L^*, a^*, and b^* were calculated using the resulting *XYZ* values. The calculation method was described in the existing studies.[37] In the experiments, distributions of color differences were plotted in the a^*–b^* chromatic plane of the CIELAB color space. Fig. 8 shows the chromaticity of the positive and negative reactions for the diagnosis of COVID-19, SARS, seasonal influenza A, and influenza A (H1N1) pdm09 after the LAMP assays were run for 30 and 60 min. The results indicate that the color of the positive and negative groups can be clearly separated in the LAMP assays, even within 30 min, for all four types of infectious diseases. Moreover, by employing the image-processing technique, the positive and negative reactions can be quantitatively assessed.

In addition, a custom-built smartphone web application for image acquisition and hue-based quantitative data analysis was developed to enable on-site diagnostics. Test results that are

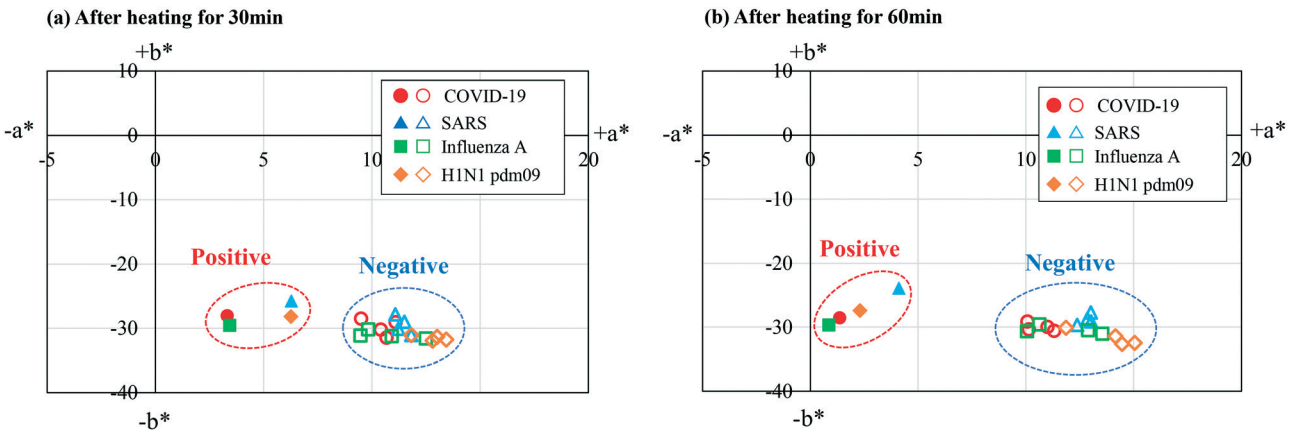

Fig. 8 Color distributions for positive (sky blue) and negative (violet) reactions after the RT-LAMP assays were performed for (a) 30 min and (b) 60 min, for the detection of SARS-CoV-2, SARS-CoV, seasonal influenza A, and influenza A (H1N1) pdm09, plotted in the a^*–b^* chromatic plane of the CIELAB color space.

either positive or negative for the simultaneous detection of four different types of infectious diseases could be automatically determined from an image acquired using a smartphone camera, as presented in Fig. S4.†

Conclusions

We developed a microfluidic flow control theory to provide design guidelines for multiplexed genetic diagnostic devices capable of sequential dispensing of samples into an array of reaction microchambers with only one operation for introducing a sample into the device. The proposed sequential liquid dispensing theory enabled us to theoretically infer the desired device specifications, such as the number of microchambers and maximal allowed flow rate, by optimizing the geometric dimensions of the microchannels and a pair of passive stop valves integrated into each microchamber. The experimental results satisfactorily agreed with the theoretically predicted number of microchambers to be dispensed at flow rates in the range of 5.0–30 μL min^{-1}.

We successfully demonstrated that the fabricated microfluidic devices enable the simultaneous diagnosis of COVID-19 (200 copies per μL) and other infectious diseases, such as SARS, seasonal influenza A, and pandemic influenza A (H1N1) 2009, which can be detected using the hue-based quantitative analysis, and the naked eye after running the colorimetric RT-LAMP assay for 30 min. In future studies, considering the 'life with corona' era, we will further develop a platform for a fast and easy sample-to-answer simultaneous diagnosis of multiple COVID-19 variants and other infectious diseases (*e.g.*, influenza viruses A and B). In principle, it is possible to flexibly customize the types of nucleic acid (DNA/RNA) targets not only for a variety of infectious diseases caused by different types of pathogens (viruses, bacteria, fungi, and parasites) for humans but also for animals, and plants, multiplexed allergen testing in food production, and multiplexed identification of poisonous plants and illegal drugs depending on their specific genetic information. Thus, this diagnostic device introduces a highly versatile technology that can be used for on-site multiplexed genetic diagnostics without a need for laborious and multiple operations. In addition, it does not require complex and expensive instrumentation across a wide range of industries, including the agriculture, food, livestock, and fisheries industries along with the health and medical care sectors.

Author contributions

Daigo Natsuhara; methodology, investigation, writing – original draft preparation, Ryogo Saito; methodology, investigation, Hiroka Aonuma; methodology, investigation, writing – review and editing, supervision, Tatsuya Sakurai; methodology, investigation, writing – review and editing, supervision, Shunya Okamoto; writing – review and editing, supervision, Moeto Nagai; writing – review and editing, supervision, Hirotaka Kanuka; writing – review and editing, supervision, funding acquisition, Takayuki Shibata; conceptualization, writing – review and editing, supervision, project administration funding acquisition. All authors have read and agreed to the published version of the manuscript.

Conflicts of interest

The authors declare no conflicts of interests.

Acknowledgements

This research was partially supported by the Japan Agency for Medical Research and Development (AMED) under Grant Number JP20he0622021. We would like to thank Editage (www.editage.com) for English language editing.

References

1 B. Hu, H. Guo, P. Zhou and Z.-L. Shi, Characteristics of SARS-CoV-2 and COVID-19, *Nat. Rev. Microbiol.*, 2021, **19**(3), 141–154, DOI: 10.1038/s41579-020-00459-7.

2 O. Vandenberg, D. Martiny, O. Rochas, A. van Belkum and Z. Kozlakidis, Considerations for diagnostic COVID-19 tests, *Nat. Rev. Microbiol.*, 2021, **19**(3), 171–183, DOI: 10.1038/s41579-020-00461-z.

3 C.-C. Lai, T.-P. Shih, W.-C. Ko, H.-J. Tang and P.-R. Hsueh, Severe acute respiratory syndrome coronavirus 2 (SARS-CoV-2) and coronavirus disease-2019 (COVID-19): The epidemic and the challenges, *Int. J. Antimicrob. Agents*, 2020, **55**(3), 105924, DOI: 10.1016/j.ijantimicag.2020.105924.

4 D.-C. Vodnar, L. Mitrea, B.-E. Teleky, K. Szabo, L.-F. Călinoiu, S.-A. Nemeș and G.-A. Martău, Coronavirus disease (COVID-19) caused by (SARS-CoV-2) infections: A real challenge for human gut microbiota, *Front. Cell. Infect. Microbiol.*, 2020, **10**, 575559, DOI: 10.3389/fcimb.2020.575559.

5 D. N. Valencia, Brief review on COVID-19: The 2020 pandemic caused by SARS-CoV-2, *Cureus*, 2020, **12**(3), e7386, DOI: 10.7759/cureus.7386.

6 B. D. Kevadiya, J. Machhi, J. Herskovitz, M. D. Oleynikov, W. R. Blomberg, N. Bajwa, D. Soni, S. Das, M. Hasan, M. Patel, A. M. Senan, S. Gorantla, J. McMillan, B. Edagwa, R. Eisenberg, C. B. Gurumurthy, S. P. M. Reid, C. Punyadeera, L. Chang and H. E. Gendelman, Diagnostics for SARS-CoV-2 infections, *Nat. Mater.*, 2021, **20**(5), 593–605, DOI: 10.1038/s41563-020-00906-z.

7 M. Rezaei, S. R. Bazaz, S. Zhand, N. Sayyadi, D. Jin, M. P. Stewart and M. E. Warkiani, Point of care diagnostics in the age of COVID-19, *Diagnostics*, 2021, **11**(1), 9, DOI: 10.3390/diagnostics11010009.

8 R. Weissleder, H. Lee, J. Ko and M. J. Pittet, COVID-19 diagnostics in context, *Sci. Transl. Med.*, 2020, **12**(546), eabc1931, DOI: 10.1126/scitranslmed.abc1931.

9 T. Parupudi, N. Panchagnula, S. Muthukumar and S. Prasad, Evidence-based point-of-care technology development during the COVID-19 pandemic, *BioTechniques*, 2020, **70**(1), 58–67, DOI: 10.2144/btn-2020-0096.

10 L. J. Carter, L. V. Garner, J. W. Smoot, Y. Li, Q. Zhou, C. J. Saveson, J. M. Sasso, A. C. Gregg, D. J. Soares, T. R. Beskid, S. R. Jervey and C. Liu, Assay techniques and test development for COVID-19 diagnosis, *ACS Cent. Sci.*, 2020, **6**(5), 591–605, DOI: 10.1021/acscentsci.0c00501.

11 Q. Song, X. Sun, Z. Dai, Y. Gao, X. Gong, B. Zhou, J. Wu and W. Wen, Point-of-care testing detection methods for COVID-19, *Lab Chip*, 2021, **21**(9), 1634–1660, DOI: 10.1039/D0LC01156H.

12 F. Palaz, A. K. Kalkan, A. Tozluyurt and M. Ozsoz, CRISPR-based tools: Alternative methods for the diagnosis of COVID-19, *Clin. Biochem.*, 2021, **89**, 1–13, DOI: 10.1016/j.clinbiochem.2020.12.011.

13 V. S. Javalkote, N. Kancharla, B. Bhadra, M. Shukla, B. Soni, A. Sapre, M. Goodin, A. Bandyopadhyay and S. Dasgupta, CRISPR-based assays for rapid detection of SARS-CoV-2, *Methods*, 2020, DOI: 10.1016/j.ymeth.2020.10.003, in press.

14 T. Notomi, H. Okayama, H. Masubuchi, T. Yonekawa, K. Watanabe, N. Amino and T. Hase, Loop-mediated isothermal amplification of DNA, *Nucleic Acids Res.*, 2000, **28**(12), e63, DOI: 10.1093/nar/28.12.e63.

15 L. Becherer, N. Borst, M. Bakheit, S. Frischmann, R. Zengerle and F. von Stetten, Loop-mediated isothermal amplification (LAMP) – review and classification of methods for sequence-specific detection, *Anal. Methods*, 2020, **12**(6), 717–746, DOI: 10.1039/c9ay02246e.

16 A. T. Scott, T. R. Layne, K. C. O'Connell, N. A. Tanner and J. P. Landers, Comparative evaluation and quantitative analysis of loop-mediated isothermal amplification indicators, *Anal. Chem.*, 2020, **92**(19), 13343–13353, DOI: 10.1021/acs.analchem.0c02666.

17 L. Mautner, C.-K. Baillie, H. M. Herold, W. Volkwein, P. Guertler, U. Eberle, N. Ackermann, A. Sing, M. Pavlovic, O. Goerlich, U. Busch, L. Wassill, I. Huber and A. Baiker, Rapid point-of-care detection of SARS-CoV-2 using reverse transcription loop-mediated isothermal amplification (RT-LAMP), *Virol. J.*, 2020, **17**(1), 160, DOI: 10.1186/s12985-020-01435-6.

18 V. L. D. Thi, K. Herbst, K. Boerner, M. Meurer, L. P. M. Kremer, D. Kirrmaier, A. Freistaedter, D. Papagiannidis, C. Galmozzi, M. L. Stanifer, S. Boulant, S. Klein, P. Chlanda, D. Khalid, I. B. Miranda, P. Schnitzler, H. G. Kräusslich, M. Knop and S. Anders, A colorimetric RT-LAMP assay and LAMP-sequencing for detecting SARS-CoV-2 RNA in clinical samples, *Sci. Transl. Med.*, 2020, **12**(556), eabc7075, DOI: 10.1126/scitranslmed.abc7075.

19 C. Yan, J. Cui, L. Huang, B. Du, L. Chen, G. Xue, S. Li, W. Zhang, L. Zhao, Y. Sun, H. Yao, N. Li, H. Zhao, Y. Feng, S. Liu, Q. Zhang, D. Liu and J. Yuan, Rapid and visual detection of 2019 novel coronavirus (SARS-CoV-2) by a reverse transcription loop-mediated isothermal amplification assay, *Clin. Microbiol. Infect.*, 2020, **26**(6), 773–779, DOI: 10.1016/j.cmi.2020.04.001.

20 F. W.-N. Chow, T. T.-Y. Chan, A. R. Tam, S. Zhao, W. Yao, J. Fung, F. K.-K. Cheng, G. C.-S. Lo, S. Chu, K. L. Aw-Yong, J. Y.-M. Tang, C.-C. Tsang, H. K.-H. Luk, A. C.-P. Wong, K. S.-M. Li, L. Zhu, Z. He, E. W. T. Tam, T. W.-H. Chung, S. C. Y. Wong, T.-L. Que, K. S.-C. Fung, D. C. Lung, A. K.-L. Wu, I. F.-N. Hung, P. C.-Y. Woo and S. K.-P. Lau, A rapid, simple, inexpensive, and mobile colorimetric assay COVID-19-LAMP for mass on-site screening of COVID-19, *Int. J. Mol. Sci.*, 2020, **21**(15), 5380, DOI: 10.3390/ijms21155380.

21 W. E. Huang, B. Lim, C.-C. Hsu, D. Xiong, W. Wu, Y. Yu, H. Jia, Y. Wang, Y. Zeng, M. Ji, H. Chang, X. Zhang, H. Wang and Z. Cui, RT-LAMP for rapid diagnosis of coronavirus SARS-CoV-2, *Microb. Biotechnol.*, 2020, **13**(4), 950–961, DOI: 10.1111/1751-7915.13586.

22 M. A. Lalli, J. S. Langmade, X. Chen, C. C. Fronick, C. S. Sawyer, L. C. Burcea, M. N. Wilkinson, R. S. Fulton, M. Heinz, W. J. Buchser, R. D. Head, R. D. Mitra and J. Milbrandt, Rapid and extraction-free detection of SARS-CoV-2 from saliva by colorimetric reverse-transcription loop-mediated isothermal amplification, *Clin. Chem.*, 2021, **67**(2), 415–424, DOI: 10.1093/clinchem/hvaa267.

23 Q.-J. Zhou, L. Wang, J. Chen, R.-N. Wang, Y.-H. Shi, C.-H. Li, D.-M. Zhang, X.-J. Yan and Y.-J. Zhang, Development and evaluation of a real-time fluorogenic loop-mediated isothermal amplification assay integrated on a microfluidic disc chip (on-chip LAMP) for rapid and simultaneous detection of ten pathogenic bacteria in aquatic animals, *J. Microbiol. Methods*, 2014, **104**, 26–35, DOI: 10.1016/j.mimet.2014.06.008.

24 S. J. Oh, B. H. Park, G. Choi, J. H. Seo, J. H. Jung, J. S. Choi, D. H. Kim and T. S. Seo, Fully automated and colorimetric foodborne pathogen detection on an integrated centrifugal microfluidic device, *Lab Chip*, 2016, **16**(10), 1917–1926, DOI: 10.1039/c6lc00326e.

25 A. Sayad, F. Ibrahim, S. M. Uddin, J. Cho, M. Madou and K. L. Thong, A microdevice for rapid, monoplex and colorimetric detection of foodborne pathogens using a centrifugal microfluidic platform, *Biosens. Bioelectron.*, 2018, **100**, 96–104, DOI: 10.1016/j.bios.2017.08.060.

26 W. Yu, Y. Chen, Z. Wang, L. Qiao, R. Xie, J. Zhang, S. Bian, H. Li, Y. Zhang and A. Chen, Multiple authentications of high-value milk by centrifugal microfluidic chip-based real-time fluorescent LAMP, *Food Chem.*, 2021, **351**, 129348, DOI: 10.1016/j.foodchem.2021.129348.

27 X. Fang, Y. Liu, J. Kong and X. Jiang, Loop-mediated isothermal amplification integrated on microfluidic chips for point-of-care quantitative detection of pathogens, *Anal. Chem.*, 2010, **82**(7), 3002–3006, DOI: 10.1021/ac1000652.

28 C. Liu, M. G. Mauk, R. Hart, M. Bonizzoni, G. Yan and H. H. Bau, A low-cost microfluidic chip for rapid genotyping of malaria-transmitting mosquitoes, *PLoS One*, 2012, **7**(8), e42222, DOI: 10.1371/journal.pone.0042222.

29 F. Sun, A. Ganguli, J. Nguyen, R. Brisbin, K. Shanmugam, D. L. Hirschberg, M. B. Wheeler, R. Bashir, D. M. Nash and B. T. Cunningham, Smartphone-based multiplex 30-minute nucleic acid test of live virus from nasal swab extract, *Lab Chip*, 2020, **20**(9), 1621–1627, DOI: 10.1039/d0lc00304b.

30 R. Wang, R. Zhao, Y. Li, W. Kong, X. Guo, Y. Yang, F. Wu, W. Liu, H. Song and R. Hao, Rapid detection of multiple respiratory viruses based on microfluidic isothermal

amplification and a real-time colorimetric method, *Lab Chip*, 2018, **18**(22), 3507–3515, DOI: 10.1039/c8lc00841h.

31 D. Natsuhara, K. Takishita, K. Tanaka, A. Kage, R. Suzuki, Y. Mizukami, N. Saka, M. Nagai and T. Shibata, A microfluidic diagnostic device capable of autonomous sample mixing and dispensing for the simultaneous genetic detection of multiple plant viruses, *Micromachines*, 2020, **11**(6), 540, DOI: 10.3390/mi11060540.

32 S. Misawa, D. Natsuhara, Y. Kiba, T. Yamamuro, R. Suzuki, T. Shibata and M. Kitamura, Rapid identification of Colchicum autumnale based on loop-mediated isothermal amplification (LAMP) assay, *Forensic Toxicol.*, 2021, **39**(1), 259–265, DOI: 10.1007/s11419-020-00557-4.

33 E. Yildirim, S. J. Trietsch, J. Joore, A. van den Berg, T. Hankemeier and P. Vulto, Phaseguides as tunable passive microvalves for liquid routing in complex microfluidic networks, *Lab Chip*, 2014, **14**(17), 3334–3340, DOI: 10.1039/c4lc00261j.

34 F. Garbarino, K. Kistrup, G. Rizzi and F. Hansen, Burst pressure of phaseguide structures of different heights in all-polymer microfluidic channels, *J. Micromech. Microeng.*, 2017, **27**(12), 125015, DOI: 10.1088/1361-6439/aa97b7.

35 M. Yamada and M. Seki, Nanoliter-sized liquid dispenser array for multiple biochemical analysis in microfluidic devices, *Anal. Chem.*, 2004, **76**(4), 895–899, DOI: 10.1021/ac0350007.

36 B. Hagmeyer, F. Zechnall and M. Stelzle, Towards plug and play filling of microfluidic devices by utilizing networks of capillary stop valves, *Biomicrofluidics*, 2014, **8**(5), 056501, DOI: 10.1063/1.4896063.

37 E. Saldaña, R. Siche, W. Castro, R. Huamán and R. Quevedo, Measurement parameter of color on yacon (Smallanthus sonchifolius) slices using a computer vision system, *LWT–Food Sci. Technol.*, 2014, **59**(2), 1220–1226, DOI: 10.1016/j.lwt.2014.06.037.

